Electronic and local structures of Mn-doped $BiFeO_3$ crystals

Y. Yoneda*
Reaction Dynamics Research Division, Japan Atomic Energy Agency, Sayo-cho, Sayo-gun, Hyogo 679-5148, Japan

Y. Kitanaka, Y. Noguchi, and M. Miyayama
Research Center for Advanced Science and Technology, The University of Tokyo, Meguro-ku, Tokyo 153-8904, Japan
(Received 13 November 2011; revised manuscript received 19 July 2012; published 27 November 2012)

The electronic structure of complex oxides is important for understanding their functional properties. Here, we report the results of investigating multiferroic $BiFeO_3$ using various x-ray spectroscopy techniques. Zn- and Mn-codoped and Mn-doped $BiFeO_3$ samples were prepared with the aim of improving ferroelectric properties of $BiFeO_3$. The valences of the doped Mn and host Fe were investigated. When oxygen vacancies exist in the sample, Mn acts as a hole acceptor. Furthermore, Mn and Fe stabilize the perovskite unit by changing their ionic radius. As a result, Mn and Fe atoms exhibit various valence states in the $BiFeO_3$ system. Evidence of the electronic structure for Fe 3*d*-O 2*p*-Bi 6*s* hybridization is also presented.

DOI: 10.1103/PhysRevB.86.184112 PACS number(s): 77.84.−s, 61.05.cj, 71.20.Be, 74.62.Dh

I. INTRODUCTION

Bismuth ferrite ($BiFeO_3$) is considered as a prototype multiferroic material and is probably the most studied of the multiferroic materials as it is the most promising candidate for realizing multiferroic devices. Although multiferroic materials have been attracting increasing interest, only the multiferroic characteristic of $BiFeO_3$ has been examined in detail. $BiFeO_3$ is also one of the most promising candidates for lead-free perovskite ferroelectrics. The crystal structure of $BiFeO_3$ has been reanalyzed recently and it was found to have a highly disordered ABO_3 perovskite-type rhombohedral structure with the space group $R3c$ (lattice parameters of $a = 5.637$ Å and $c = 13.802$Å).[1,2] The mechanism for its ferroelectricity essentially originates from the long-range ordering of dipolar moments on the Bi site. The spontaneous polarization (P_s) of $BiFeO_3$ was calculated to be 84 $\mu C/cm^2$.

One of the main problems of $BiFeO_3$ is the high leakage current, which has been attributed to the small amounts of Fe^{2+} ions and oxygen vacancies existing in samples.[3,4] Despite the many reports on $BiFeO_3$, the effects of oxygen stoichiometry have not been investigated sufficiently. Only few papers have recently been published on the effects of oxygen content on the properties of $BiFeO_3$.[5,6] Mn substitution has been used to decrease the leakage current of $BiFeO_3$ so that Mn may become a hole acceptor. Furthermore, Mn substitution plays an important role in impurity-induced domain switching. Pure $BiFeO_3$ single crystal has a very small P_s owing to a large coercive electric field (E_c). However, P_s for $BiFeO_3$ can be increased by the same manner as for $PbTiO_3$ single crystal. Since E_c for $PbTiO_3$ single crystal is extremely large, one can hardly observe the P-E hysteresis loop for $PbTiO_3$ single crystal. A polarization switching is established through the nucleation of ferroelectric domains around defects and subsequent domain wall motion.[7,8] When Mn and W are substituted for Ti, the substituted Mn and W act as nuclei in for domain switching. As a result, Mn- and W-codoped $PbTiO_3$ single crystal exhibits a highly-saturated P-E hysteresis loop. In $BiFeO_3$, Zn and Mn atoms are substituted for Fe, and act as nuclei in domain switching. When the Mn and Zn are substituted in high-quality $BiFeO_3$ crystal, Mn exhibits different behavior. Mn is a transition metal and the substituted Mn has various valence states depending on the environment, such as the presence of oxygen deficiency.[9]

Hai *et al.* performed a first-principles study on $BiFe_{1-x}Mn_xO_3$ ($0 \leqslant x \leqslant 0.5$) and reported that Mn ions have an oxidation state of +3.[10] Selbach *et al.* studied experimentally on $BiFe_{1-x}Mn_xO_{3+\delta}$ ($0 \leqslant x \leqslant 0.3$) and reported the valence state of Mn is +3 and excess oxygen is compensated by partial oxidation of Mn^{3+} to Mn^{4+}.[11,12] Kothari *et al.* performed Mössbauer and x-ray photoelectron spectroscopy (XPS) and also reported that Mn ions have an oxidation state of +3.[13] Higuchi *et al.* performed x-ray absorption spectroscopy (XAS) using Mn 2*p* and obtained the same result.[14] Since the valence number of Fe is +3, the valence state of the host $BiFeO_3$ is compensated by substituting Mn^{3+} for Fe^{3+}. On the other hand, there have been some reports of the existence of other valence states of Mn. If the valence states of Bi^{3+}, Fe^{3+}, and O^{2+} ions deviate from their formal values, then that of the substituted Mn also deviates. Kumar and Yadav suggested that Mn ions have a valence state of +4 to reduce the number of oxygen vacancies and to increase the resistivity.[15] Mn has a different valence in codoped and solid-solution systems. Anjum *et al.* reported that Mn ions exist with a valence state of +3 and a small contribution of +2 and +4 in Zn- and Mn-codoped $BiFeO_3$.[16] Kawae *et al.* reported the valence state of +2 when Mn is substituted in $BiFeO_3$–$BaTiO_3$ solid solution and Mn- and Ti-codoped $BiFeO_3$.[17,18] Furthermore, we have shown the occurrence of a chemical shift of the absorption edge of the host Fe in Mn-doped $BiFeO_3$ and $PbTiO_3$-$BiFeO_3$ solid solution.[19] The electronic structure of the host Fe is also affected by the substitution of Mn. Owing to the difficulty of synthesis, oxygen vacancies are easily generated in $BiFeO_3$, and also cause the valence fluctuation of Fe and substituted Mn atoms. Thus we require high-quality Mn-doped $BiFeO_3$ with little oxygen deficiency.

Here we again confirm the effect of Mn substitution in stoichiometric $BiFeO_3$. In this work, we prepared single crystals of Zn- and Mn-codoped $BiFeO_3$ and Mn-doped $BiFeO_3$ crystals and investigated their electronic and local structures

using various x-ray spectroscopy techniques. Investigating the electronic structural changes of these heterovalent- and/or isovalent-ion-doped $BiFeO_3$ samples provides important information about the Mn substitution mechanism. It was found that the valence state of the substituted Mn was different from that reported in Ref. 16 ($La_{0.8}Bi_{0.2}Fe_{1-x}Mn_xO_3$) and in Ref. 20 ($BiFe_{0.95}Mn_{0.05}O_3/BiFe_{0.95}Zn_{0.05}O_3$ bilayer film). The electronic structure is greatly changed by annealing. It is necessary to consider Fe $3d$–O $2p$–Bi $6s$ hybridization to explain the valence states of the Mn-substituted $BiFeO_3$.

II. EXPERIMENTAL

Details of the sample preparation are given in Refs. 5 and 9. Essentially, single-crystal samples of Mn-doped $BiFeO_3$ and Zn- and Mn-codoped $BiFeO_3$ were prepared by the self-flux method in Ar flow. High-purity powders of Bi_2O_3 (99.9999%), Fe_2O_3 (99.99%), ZnO (99.99%), and Mn_2O_3 (99.99%) were used as raw materials. They mixed at a molar ratio Bi : Fe : Mn = 1 : 1 : 0.01 in Mn-doped $BiFeO_3$ and Bi : Fe : Zn : Mn = 1 : 1 : 0.005 : 0.005 in Zn- and Mn-codoped $BiFeO_3$. The start materials were sintered at 880 °C and then mixed with flux composed of Bi_2O_3 and B_2O_3. The mixtures soaked at 850 °C and then cooled slowly to room temperature. Single crystals with a maximum size of 3 × 3 × 0.1 mm were obtained. These crystals were annealed at 830 °C for 2 h in air before electrical and magnetic measurements.

The chemical composition of the crystals was determined by inductively coupled plasma atomic emission spectrometry (ICP-AES). The observed chemical composition is $BiFe_{0.995}Mn_{0.005}O_3$ for Mn-doped sample and $BiFe_{0.99}Zn_{0.005}Mn_{0.005}O_3$ for Zn- and Mn-codoped sample. The phase, structure and crystalline quality of the $BiFeO_3$ single crystals were analyzed by laboratory x-ray diffraction measurements using Cu-K_α radiation. There was no large difference in a lattice parameter by a sample. The lattice parameters of a and c in a rhombohedral structure of these four samples were $a = 5.565$ Å and $c = 13.93$ Å. For electrical characterization, the crystals were sliced and gold electrodes were sputtered. Polarization (P) and electric-field (E) hysteresis loops were measured by using a FCE-1 ferroelectric test system (Toyo Co. Ltd.) in the virtual ground mode at a frequency of 1 Hz at 25 °C. Polarization switching current density (J_{sw}) was calculated from the values of P measured during the hysteresis loops. Leakage current density (J_{leak}) was also measured during applying a constant E. The step of E was 2.5–5 kV/cm, and the value of J_{leak} was measured after an elapsed time of 30 s from an increase in E. dc magnetization measurements were performed with a SQUID magnetometer (Quantum Design MPMS). Magnetization-applied field (M-H) curves were measured between 2 and 400 K in field cooled (FC) and zero-field cooled (ZFC) methods with an applied field (H) of 1000 Oe.

The valence of Mn in oxides at the sample surface tends to be +2, because Mn reduces easily. Soft x rays are unsuitable for XPS because of their narrow working distance from the surface. We performed x-ray spectroscopy using hard x rays to detect the bulk-sensitive electronic states. X-ray absorption fine structure (XAFS) spectra were measured at BL14B1 of SPring-8, which is a bending-magnet beamline dedicated to Japan Atomic Energy Agency equipped with a double-crystal monochromator. A pair of Si (311) crystals were used for both the first and second crystals and the x-ray beam was provided by an inclined (111) net plane. For the first crystal, a directly fin-cooled crystal was used. A sagittal focus bender (Kohzu Precision Co.) was used to increase the x-ray photon flux density at the sample position.[21] The focused beam size was 1-mm height × 3-mm width. The XAFS spectra were obtained by recording the fluorescence yield for Mn-K edge and the absorption for Bi-$L3$ and Fe-K edges. Each XAFS spectrum was obtained with 0.5 eV resolution and normalized to the incident x-ray beam. The extended x-ray absorption fine structure (EXAFS) oscillation part $k^3\chi(k)$ was extracted from the observed absorption spectrum using the McMaster equation and the cubic spline method.[22,23] $k^3\chi(k)$ was Fourier transformed in the range of 12 $Å^{-1}$ to evaluate the radial distribution function. X-ray emission spectroscopy (XES) is a classical technique for studying the electronic structure of bulk samples, for which it is ideally suited owing to the possibility of obtaining information at a large depth. Fe-K XES was performed using a laboratory x-ray source. The Fe-K emission spectrum was collected with a double-crystal spectrometer fabricated by Rigaku Co. of Japan.[24] The crystal structure was drawn using the program VESTA.[25]

III. RESULTS

A. Electrical and magnetic measurements

Basically, pure $BiFeO_3$ without oxygen deficiency and without Bi deficiency has a low leakage current, as shown in Fig. 1. The low leakage current is a evidence of high-quality $BiFeO_3$ crystal without defects or impurities. Since Zn^{2+} ions are substituted for Fe^{3+}, Zn-doped $BiFeO_3$ ($BiFe_{0.995}Zn_{0.005}O_3$) has a high leakage current. Zn^{2+} is substituted for the Fe^{3+} according to the following equation: $2ZnO = 2Zn_{Fe'} + 2O_O{*} + V_O^{\bullet\bullet}$, where $Zn_{Fe'}$ is Zn^{2+} at the Fe^{3+} site and $O_O{*}$ is O^{2-} at the O site. Zn^{2+} substitution leads to the formation of $V_O^{\bullet\bullet}$ (doubly ionized oxygen vacancy) because of

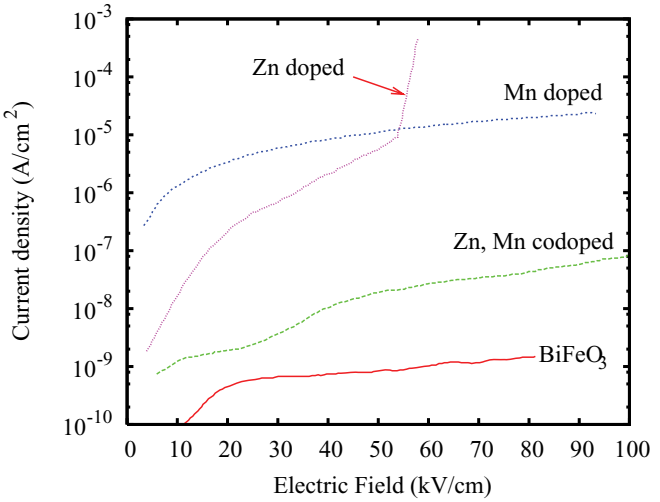

FIG. 1. (Color online) Leakage current densities of Zn- and Mn-codoped, Mn-doped, Zn-doped, and pure $BiFeO_3$ crystals after annealing in air.

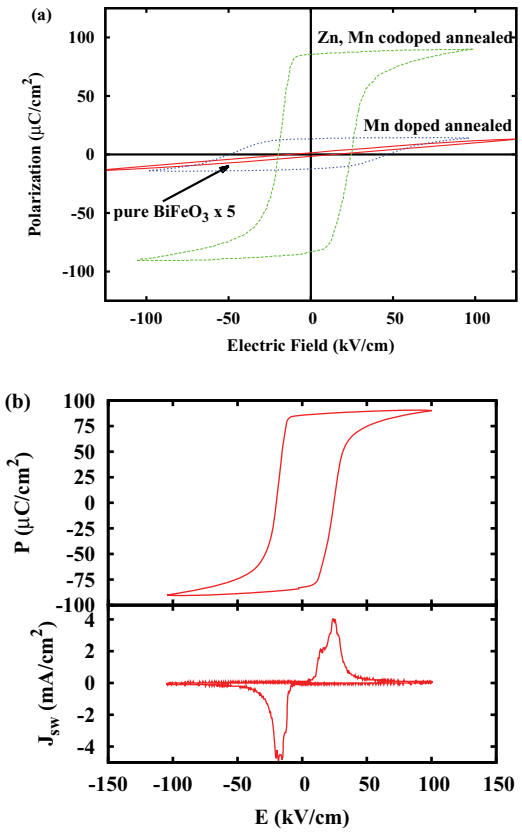

FIG. 2. (Color online) (a) Polarization-electric field (P-E) hysteresis loops of pure (solid line), Zn- and Mn-codoped (dotted line), and Mn-doped (dashed line) $BiFeO_3$ crystals after annealing in air. (b) P-E hysteresis loop (upper) and switching current response (lower) of Zn- and Mn-codoped $BiFeO_3$ crystal.

the charge neutrality restriction. Annealing in air after crystal growth results in the oxidation reaction given by the equation: $V_O^{\bullet\bullet} + 1/2O_2 \leftrightarrow O_O{*} + 2h^{\bullet}$, where $h^{\bullet}$ is an electron hole. Zn^{2+} substitution increases $V_O^{\bullet\bullet}$ and $h^{\bullet}$, and this is responsible for the high leakage current. In Mn-doped and Zn- and Mn-codoped $BiFeO_3$ crystals, it is possible that Mn atoms are substituted as Mn^{2+}, Mn^{3+}, or Mn^{4+}. If the Mn atoms are substituted while maintaining the charge compensation, the leakage property of the doped $BiFeO_3$ will be the same as that of pure $BiFeO_3$. However, the Mn-doped and Zn- and Mn-codoped $BiFeO_3$ crystals have a higher leakage current than pure $BiFeO_3$. Thus the Mn valence deviates from +3 in Mn-doped $BiFeO_3$, and from +4 in Zn- and Mn-codoped $BiFeO_3$. Figure 2(a) shows the observed P-E hysteresis loops of the pure, Mn- and Zn-codoped, and Mn-doped $BiFeO_3$ single crystals after thermal treatment. Although the leakage current density is very low in the pure $BiFeO_3$, only tiny polarization reversal was observed. On the other hand, fully saturated loop was observed in Zn- and Mn-codoped $BiFeO_3$. These loops were measured with no compensation. Raw switching current response (J_{sw}) of Zn- and Mn-codoped $BiFeO_3$ is shown in Fig. 2(b). Since the substituted atoms act as nuclei in domain switching, the Mn-doped and Zn- and Mn-codoped $BiFeO_3$ crystals exhibit highly saturated hysteresis loops. However, the magnitude of P_s is different for the two samples. P_s for Zn- and Mn-codoped $BiFeO_3$ is seven times larger than that of Mn-doped $BiFeO_3$. Polarization properties improved drastically by Zn- and Mn-codoping. For Zn- and Mn-codoped crystals, the values of J_{sw} are in the range of $10^{-5} \sim 4\times10^{-3}$ A/cm^2, which is at least two orders of magnitude higher than those of J_{leak}. These results demonstrate that the P-E hysteresis loop observed for Zn- and Mn-codoped $BiFeO_3$ originates from ferroelectric nature, i.e., the switching of P_s, and is not influenced by J_{leak}. The values of J_{leak} for Mn-doped $BiFeO_3$ were of the order of 10^{-5} A/cm^2 at a higher E, which are comparable to those of J_{sw}. Thus the P-E hysteresis loop for Mn-doped $BiFeO_3$ is affected to some extent by J_{leak}, leading to an overestimation of its P_r value. The value of P_s was strongly dependent on the dopant concentration. It is known that negatively and positively charged defects form a defect dipole at an adjacent site because of the minimization of electrostatic energy in ferroelectric crystals.[26] It is expected that a defect dipole composed of Zn and Mn is present in Zn- and Mn-codoped crystals. The Zn- and Mn-codoped $BiFeO_3$ is the best composition to observe the large P-E loop. However, dopants act the nuclei for domain switching only when the small Bi and O deficiency.

Figure 3(a) shows the M-H isotherm curves of the Zn- and Mn-codoped and Mn-doped $BiFeO_3$ single crystals with applied magnetic field of 1000 Oe. Both samples produced curves indicating antiferromagnetism. The magnetization for Zn- and Mn-codoped $BiFeO_3$ rapidly increases below 50 K, as shown in Fig. 3(b). Transitions with different spin, charge,

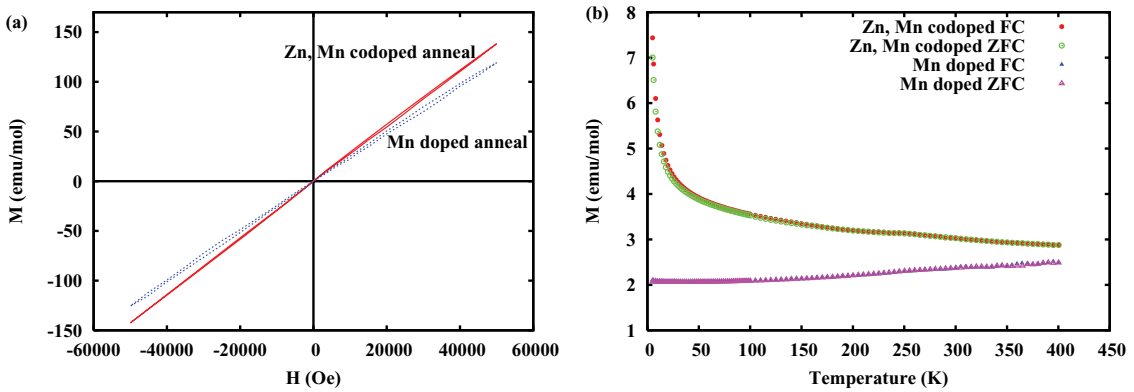

FIG. 3. (Color online) (a) Magnetization-applied field (M-H) isotherm curves of Zn- and Mn-codoped (solid line) and Mn-doped (dashed line) $BiFeO_3$ crystals after annealing in air. (b) FC and ZFC M-T curves for Zn- and Mn-codoped and Mn-doped $BiFeO_3$ crystals.

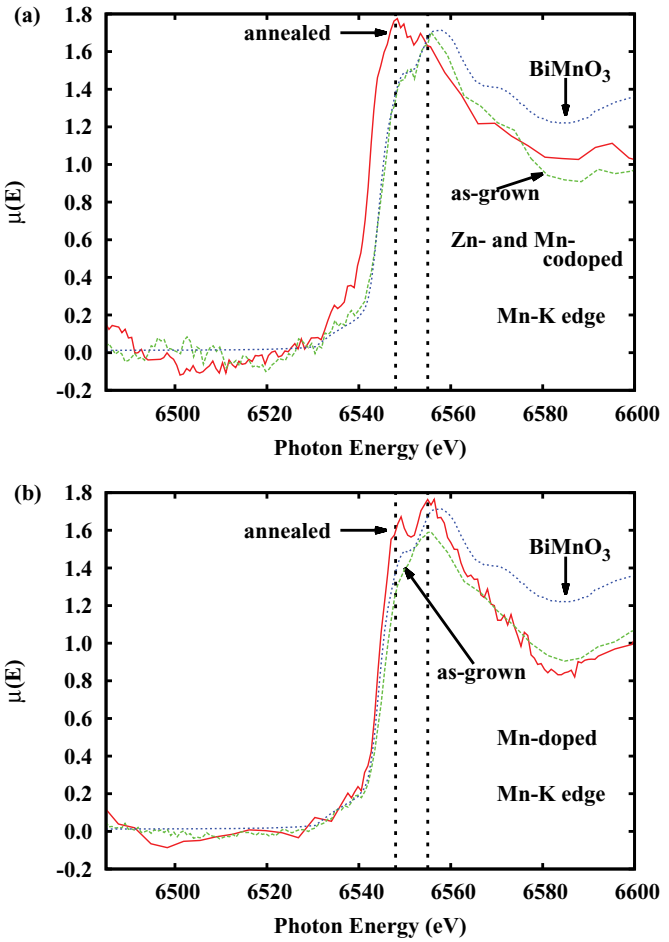

FIG. 4. (Color online) Mn-K edge XAFS spectra of (a) Zn- and Mn-codoped $BiFeO_3$ and (b) Mn-doped $BiFeO_3$. Pure $BiMnO_3$ crystal was also observed as the Mn^{3+} reference.

and orbital orderes exists in $BiFeO_3$ as well as $BiMnO_3$, and they are affected by substitutions. For example, orbital order temperature of $Bi(Mn_{0.95}Gd_{0.05})O_3$ is 60 K lower than that of pure $BiMnO_3$[27] and similar behavior have been found in $BiMn_{1-x}Cr_xO_3$.[28,29] The reduce of magnetic transition temperature in Zn- and Mn-codoped $BiFeO_3$ took place according to the similar substitution effect. This result is in agreement with the highly-saturated P-E hysteresis loop of Zn- and Mn-codoped $BiFeO_3$ owing to the impurity-induced domain switching.

B. Mn-K edge XAFS

Mn-K edge XAFS spectra were obtained by measuring the fluorescence yield. Figure 4 shows the XAFS spectra of the doped $BiFeO_3$ crystals and pure $BiMnO_3$ around the absorption energy of Mn ($E = 6539$ eV). Although the Mn composition of these crystals was 0.5%, sufficiently strong signals were obtained to determine the valence number of Mn ions. There are two types of x-ray absorption near-edge structure (XANES) as indicated by dashed lines. The peak located at the lower energy of 6548 eV is related to Mn^{2+}. The XANES spectrum of Zn- and Mn-codoped $BiFeO_3$ after annealing includes the Mn^{2+} component. The other peak located at a higher energy of 6555 eV is related to Mn^{3+}. This component was observed in three samples: Zn- and Mn-codoped $BiFeO_3$ before annealing and Mn-doped $BiFeO_3$ crystals before and after annealing. In particular, the XANES spectra of the Zn- and Mn-codoped as-grown and annealed Mn doped $BiFeO_3$ samples are similar to the reference $BiMnO_3$ spectrum. The major component is Mn^{3+} in these two samples. In Zn- and Mn-codoped as-grown, and Mn-doped annealed samples, hole carrier exists owing to charge compensation of oxygen deficiency, and owing to $Fe^{3+} \leftrightarrow Fe^{2+}$ valence change. When the hole carrier exists, Mn act as a strong hole acceptor and it substituted Mn^{3+} for Fe^{3+} site. One can easily distinguish Mn^{2+} and Mn^{3+} because the XANES spectrum of Mn^{2+} is greatly different from that of Mn^{3+}. In contrast, the XANES spectra of Mn^{3+} and Mn^{4+} are almost the same but the absorption energy is slightly different. We also measured XANES spectra of pure $BiMnO_3$ as Mn^{3+} reference. We can distinguish Mn^{3+} and Mn^{4+} by the shift of absorption edges. In this case, the absorption edges of Zn- and Mn-codoped as-grown $BiFeO_3$ and Mn-doped annealed $BiFeO_3$ are located at the same energy. The trace of Mn^{4+} was not found. Thus Mn^{3+} contributes the spectra of the three samples. The Mn^{3+} component decreased and the absorption edge shifted toward a lower energy with increasing Mn^{2+} component. Table I shows the valence states of Mn atoms obtained by Mn-K XAFS. We expected that the Mn valence states would be +4 in the Zn- and Mn-codoped sample and +3 in the Mn-doped sample because of charge compensation. However, the Mn valence in Zn- and Mn-codoped $BiFeO_3$ after annealing deviated from +4. From the Mn-K edge XAFS measurements, it is estimated that oxygen deficiency also increases by Mn substitution according to the following equation: $2Mn_2O_3 = 2Mn_{Fe'} + 2O_O + V_O^{\bullet\bullet} + O_2$ Mn^{2+} substitution increases $V_O^{\bullet\bullet}$ and $h^\bullet$. $h^\bullet$ is trapped by hole acceptor of Mn^{2+}, then Mn^{2+} changed to Mn^{3+}. Furthermore, although the Mn valence state in Mn-doped $BiFeO_3$ was +3, the leakage current of Mn-doped $BiFeO_3$ was higher than that of Zn- and Mn-codoped $BiFeO_3$. This clearly indicates that the leakage property is not determined only by the Mn valence. We require further information on the electronic structures of Fe and Bi to clarify the relationship between the leakage property and Mn valence.

TABLE I. Summary of Mn and Fe valence states.

Sample	Mn-K Abs. edge (eV)	Mn valence	Fe^{3+} : Fe^{2+} ratio
Zn- and Mn-codoped annealed	6542.06	Mn^{2+}	10:0
Zn- and Mn-codoped as-grown	6545.13	Mn^{3+}	4:1
Mn-doped annealed	6545.75	Mn^{3+}	6:1
Mn-doped as-grown	6544.29	$Mn^{2+} + Mn^{3+}$	4:1

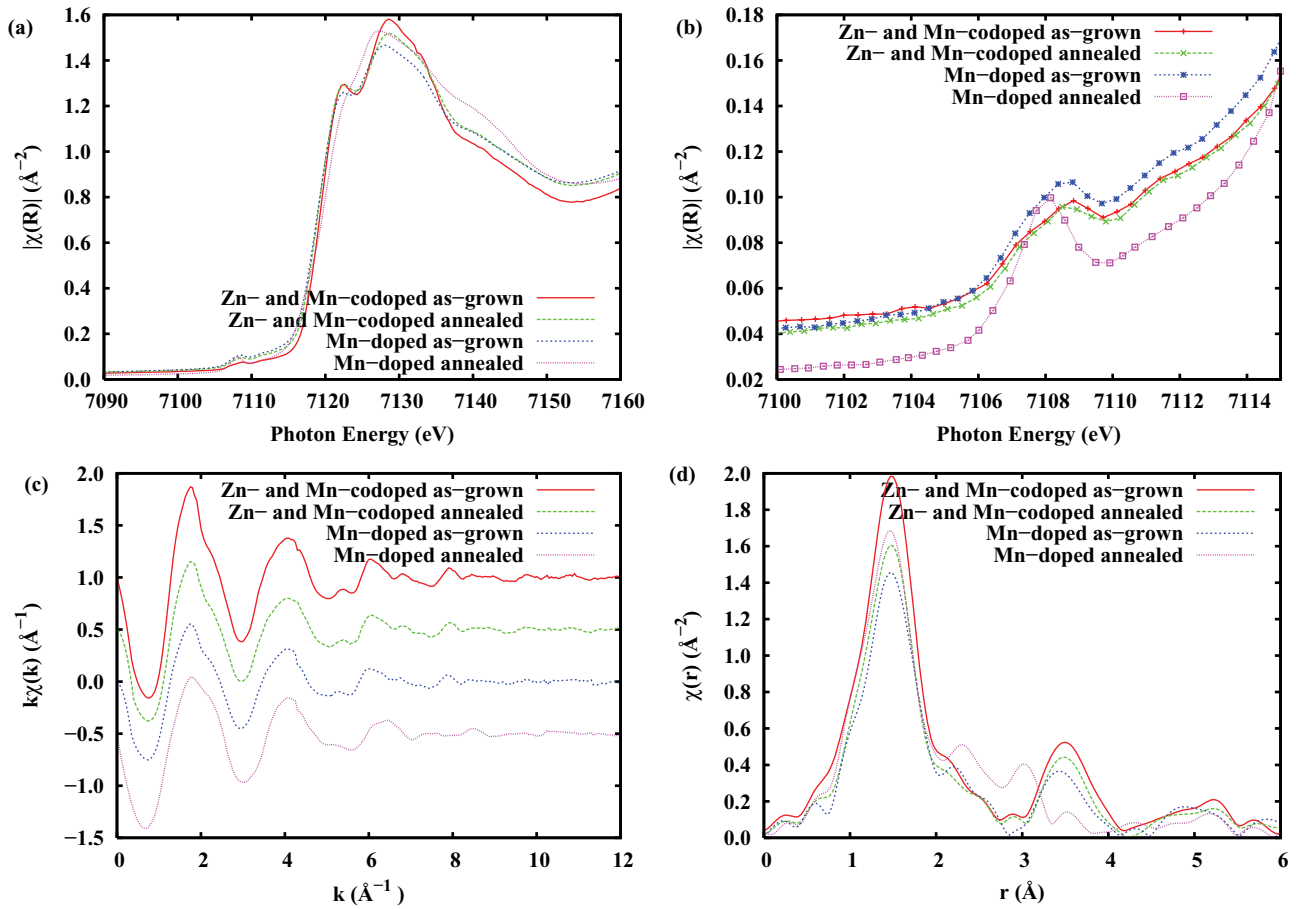

FIG. 5. (Color online) (a) Fe-K XANES spectra of $BiFeO_3$ crystals of Zn- and Mn-codoped $BiFeO_3$ before annealing, Zn- and Mn-codoped $BiFeO_3$ after annealing, Mn-doped $BiFeO_3$ before annealing, and Mn-doped $BiFeO_3$ after annealing. (b) Pre-edge spectra of $BiFeO_3$ crystals. (c) EXAFS functions extracted from Fe-K XAFS spectra of $BiFeO_3$ crystals. The data were offset for clarity. (d) Radial distribution functions without phase correction. The obtained bond distances are shown in Table II.

C. Fe-K edge XAFS

Fe-K edge XAFS spectra are shown in Fig. 5(a). The Fe-K edges of the $BiFeO_3$ crystals were located at the same energy except for that of Mn-doped annealed $BiFeO_3$. The pre-edge shape of Mn-doped annealed $BiFeO_3$ was also different from that of the other samples, as shown in Fig. 5(b). The first-nearest-neighbor bond distribution around Fe atoms was examined by EXAFS analysis. Figure 5(c) shows the extracted EXAFS functions of the $BiFeO_3$ crystals. The EXAFS function of the Mn-doped annealed sample at approximately 2 Å^{-1} has a different shape from those of the other samples. Figure 5(d) shows the radial distribution functions of the doped $BiFeO_3$ crystals. The calculated Fe–O bond distances are shown in Table II. The resolution of XAFS analysis is approximately 0.01 Å. The Fe–O bond distance of Zn- and Mn-codoped $BiFeO_3$ slightly changed through annealing. On the other hand, Fe–O distance of Mn-doped $BiFeO_3$ decreased by annealing. The change of bond distance through annealing is mainly depended on the oxygen deficiency. The oxygen vacancy introduces a repulsion force around the vacancy site. The repulsion force reduced, as oxygen vacancies are decreased by annealing. The small change of the bond distance in the Zn- and Mn-codoped $BiFeO_3$ indicates the small amount of oxygen vacancy even in the as-grown sample. The results of Mn valence is also consistent with the Fe–O bond distance by concerning the ionic radius as listed in Table III.[30] The repulsion force due to oxygen vacancy reduced, but bond distance kept by the larger Mn^{2+}- and Zn^{2+}-substitution for Fe^{3+} in the Zn- and Mn-codoped $BiFeO_3$. The change of Fe–O bond distance through annealing in Mn-doped $BiFeO_3$ is larger than that in Zn- and Mn-codoped $BiFeO_3$. Since Mn^{3+} with the same ionic radius substituted for Fe^{3+}, Fe–O bond distance decreased as the repulsion force due to oxygen vacancy reduced. The as-grown samples of Zn- and Mn-codoped and Mn-doped $BiFeO_3$ appear to have the same local structure and the same electronic structure, but they exhibit different

TABLE II. Summary of nearest-neighbor bond distances.

Sample	Fe–O distance (Å)	Bi–O distance (Å)
Zn- and Mn-codoped annealed	2.01	2.37
Zn- and Mn-codoped as-grown	2.00	2.37
Mn-doped annealed	1.97	2.39
Mn-doped as-grown	2.02	2.40

TABLE III. Ionic radii of *B*-site ions.[30]

B-site ion	r_B (Å)
Zn^{2+}	0.75
Mn^{2+}	0.83
Mn^{3+}	0.64
Fe^{2+}	0.78
Fe^{3+}	0.64

behavior after annealing. Although the electronic structure of Zn- and Mn-codoped $BiFeO_3$ did not change significantly upon annealing, both the electronic and local structures changed in Mn-doped $BiFeO_3$. The valence band of $BiFeO_3$ consists of the O 2*p* state hybridized with the Fe 3*d* state.[31,32] When the Fe–O bond distance changes, the Fe–O hybridization should also be changed. Similar behavior occurs in the perovskite oxides, which include transition-metal oxides, such as $LaMnO_3$[33] and $CaFeO_3$[34]. In these materials, the effect of metal-oxygen covalent bonding appears as competition between Jahn-Teller distortion and charge disproportionation. The Jahn-Teller distortion of the MnO_6 or FeO_6 octahedron changes with the changing hybridization between *B*-site atoms and oxygen atoms. The change in the Fe environment may be caused by the change in hybridization between the Fe ion and O cation.[35–37]

D. Bi-*L*3 edge XAFS

The electronic and local structures of Bi atoms were also examined in the same manner. Figure 6(a) shows the Bi-*L*3 XANES spectra of the $BiFeO_3$ crystals. Although the absorption edges lie at approximately the same energy, the XAFS spectrum of Mn-doped annealed $BiFeO_3$ has a different shape from those of the other samples. Figure 6(b) shows the same XANES spectra with a different scale. The absorption edges of the Mn-doped before and after annealed and the Zn- and Mn-codoped after annealed samples lie at the same energy, and the valence number of the Bi ions is assigned to +3. On the other hand, the absorption energy of the Zn- and Mn-codoped sample before annealing shifted to a slightly lower energy. Since Mn^{2+} and Zn^{2+} ions are substituted for Fe^{3+} in the Zn- and Mn-codoped sample, the shift of the absorption edge of Bi is caused by heterovalent-ion substitution. The $BiFeO_3$ samples exhibited different behavior upon annealing. In the Zn- and Mn-codoped sample, the absorption edge shifted but the shape of the XANES spectrum did not change. In the Mn-doped samples, the absorption edge did not shift but the shape of the XANES spectrum changed. The EXAFS functions were extracted, as shown in Fig. 6(c). All the EXAFS functions except for that of Mn-doped annealed $BiFeO_3$ are similar. The radial distribution functions of the samples are shown in Fig. 6(d). The Bi–O bond distances are shown in Table II.

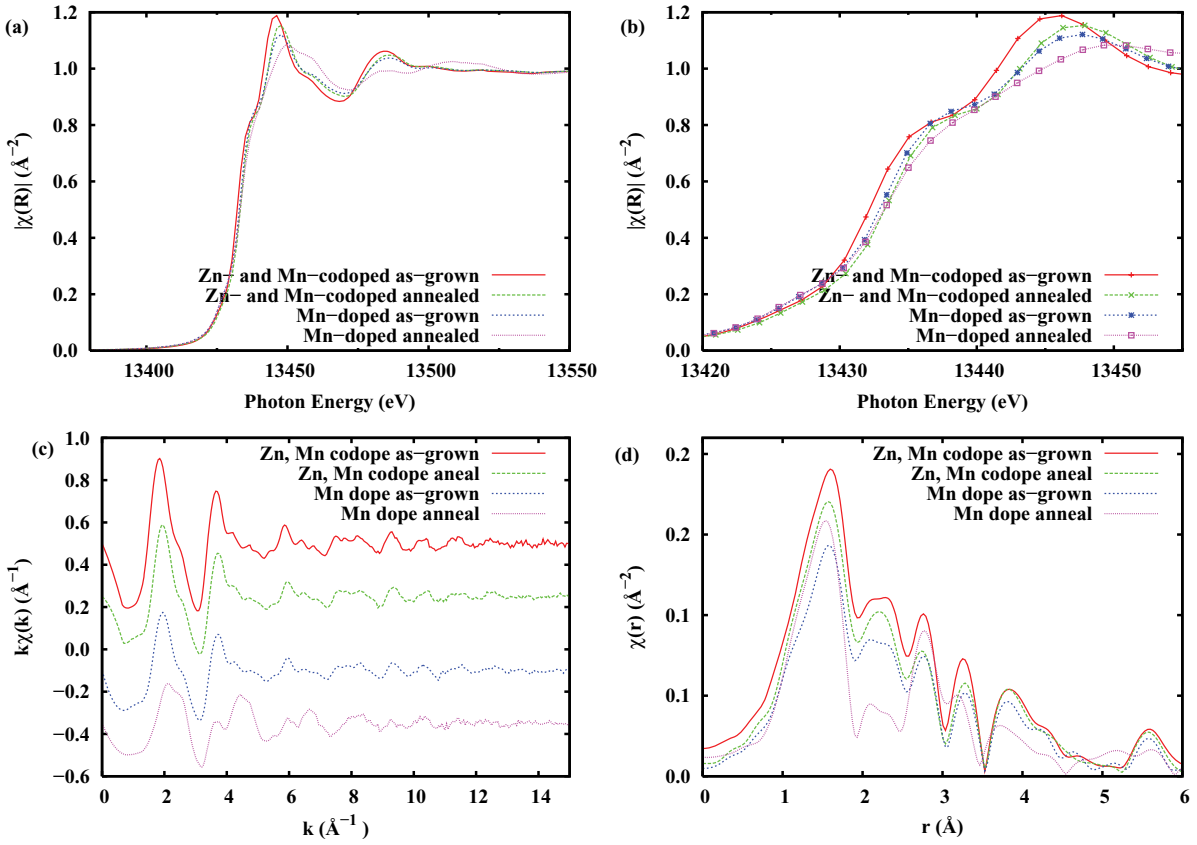

FIG. 6. (Color online) (a) Bi-*L*3 XANES spectra of $BiFeO_3$ crystals of Zn- and Mn-codoped $BiFeO_3$ before annealing, Zn- and Mn-codoped $BiFeO_3$ after annealing, Mn-doped $BiFeO_3$ before annealing, and Mn-doped $BiFeO_3$ after annealing. (b) Preedge spectra of $BiFeO_3$ crystals. (c) EXAFS functions extracted from Bi-*L*3 XAFS spectra of $BiFeO_3$ crystals. The data were offset for clarity. (d) Radial distribution functions without phase correction. The obtained bond distances are shown in Table II.

Although the first-nearest-neighbor distances of the four samples are almost the same, Mn-doped annealed $BiFeO_3$ has a different local structure, particularly in the large-r region including the second-nearest-neighbor and higher bond distances. Since the repulsion force due to the oxygen vacancy should be influenced locally just around the vacancy site, Fe–Fe distance is elongated by the repulsion force. Fe–O distance is influenced larger compared to Bi–O distance, because Fe–O is the nearest neighbor from the vacancy site. On the other hand, Bi–O bond has a smaller covalency than Fe–O bond, and is the second-nearest neighbor from the vacancy site. Thus Bi–O bond distribution is influenced slightly by the oxygen vacancy.

It is estimated that the Bi–O bond distance of $BiFeO_3$ is shorter than that of the other bismuth oxides such as $Bi_4Ti_3O_{12}$. Although the high-temperature paraelectric phase of $Bi_4Ti_3O_{12}$ can be observed at 700 °C,[38] $BiFeO_3$ decomposed around the phase transition temperature of 850 °C owing to its tight tolerance.[2] The covalent character of the Bi–O bond in $BiFeO_3$ is not negligible owing to the Bi–O hybridization. We found the possibility of a change in the hybridization between Fe–O from the Fe-K XAFS measurements. We also observed the hybridization between Bi and O. The change in the hybridization due to annealing was considerable in Mn-doped $BiFeO_3$. Thus competition between Jahn-Teller distortion and charge disproportionation in the Bi $2p$–O $6s$–Fe $3d$ system is also possible. The XANES signals are affected not only by the electronic structure but also by the local structure. The local structure of Mn-doped $BiFeO_3$ was found to be different from that of Zn- and Mn-codoped $BiFeO_3$. It is difficult to estimate the valence state of the Fe ion when the local structure changes. We require further information to determine the valence state of the iron atoms.

E. Fe-K edge XES

We performed XES measurements of the Fe-Kα1 and Fe-Kα2 spectra of the doped $BiFeO_3$ crystals to estimate the effective valence number of iron atoms. Figures 7(a) and 7(b) show the XES spectra of Zn- and Mn-codoped $BiFeO_3$ before and after annealing, and Figs. 7(c) and 7(d) show the XES spectra of Mn-doped $BiFeO_3$ before and after annealing, respectively. We also measured the spectra of $FeTiO_3$ and Fe_2O_3 as reference samples. The valence states of $FeTiO_3$ and Fe_2O_3 were Fe^{2+} and Fe^{3+}, respectively. The valence state of Fe in the doped $BiFeO_3$ samples was estimated by the deconvolution of the XES profiles of the Fe_2O_3 and $FeTiO_3$ reference samples. The ratios of Fe^{2+} and Fe^{3+} in the doped $BiFeO_3$ samples were listed in Table I. Before annealing, the main component of the XES spectrum of Zn- and Mn-codoped $BiFeO_3$ was Fe^{3+}, but the Fe^{2+} component was also observed,

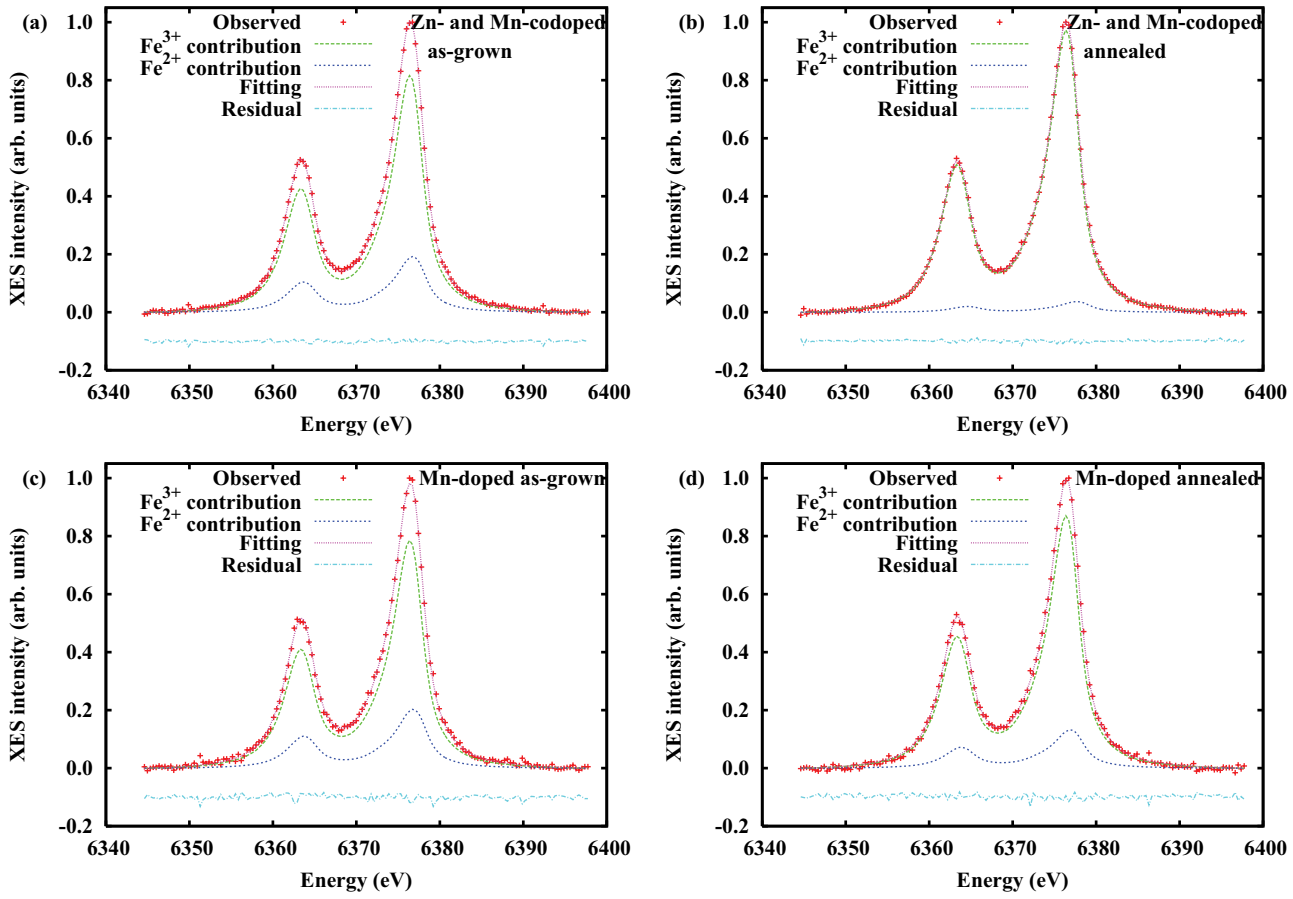

FIG. 7. (Color online) Fe-Kα1 ($E = 6377$ eV) and Fe-Kα2 ($E = 6263$ eV) spectra of $BiFeO_3$ crystals. (a) Zn- and Mn-codoped $BiFeO_3$ before annealing. (b) Zn- and Mn-codoped $BiFeO_3$ after annealing. (c) Mn-doped $BiFeO_3$ before annealing. (d) Mn-doped $BiFeO_3$ after annealing. The valence state of the Fe ion was estimated by deconvolution of the reference Fe_2O_3 (for Fe^{3+}) and $FeTiO_3$ (for Fe^{2+}) profiles. The obtained Fe^{3+} : Fe^{2+} ratios are shown in Table I.

as shown in Fig. 7(a). After annealing, the Fe^{2+} component disappeared and the observed XES spectrum was composed almost entirely of the Fe^{3+} component, as shown in Fig. 7(b). In Mn-doped $BiFeO_3$, before annealing the XES spectrum consisted of both Fe^{3+} and Fe^{2+} components, as shown in Fig. 7(c). After annealing, the Fe^{3+} component increased in intensity, but the Fe^{2+} component still existed, as shown in Fig. 7(d). In Mn-doped $BiFeO_3$, most of the Fe^{2+} ions did not change to Fe^{3+} ions and remained as Fe^{2+}. The ratio of Fe^{2+} to Fe^{3+} intensities was almost the same in the as-grown Zn- and Mn-codoped and as-grown Mn-doped $BiFeO_3$ crystals but it was different in the annealed samples. Since the oxygen deficiency decreased in the annealing process, Fe^{2+} changed to Fe^{3+} in Zn- and Mn-codoped $BiFeO_3$. On the other hand, Fe^{2+} can exist in Mn-doped annealed $BiFeO_3$ because the local environment of Mn-doped $BiFeO_3$ is different from that of Zn- and Mn-codoped $BiFeO_3$ owing to the Bi $6s$–O $2p$–Fe $3d$ hybridization. It is safe to say that the Fe^{2+}/Fe^{3+} ratio is closely connected with the leakage properties.

F. Local structure analysis

The Zn- and Mn-codoped and Mn-doped $BiFeO_3$ samples had similar electronic and local structures before annealing. They changed after annealing, particularly in the second-nearest-neighbor range. We performed local structure analysis of the annealed samples in the second-nearest-neighbor range.

In the Fe-K XAFS spectrum, the first-nearest-neighbor distance of Fe–O did not vary greatly, but a difference between the Zn- and Mn-codoped and the Mn-doped samples appeared at approximately $2 \leqslant r \leqslant 4$ Å, as shown in Fig. 5(d). The fitting result of the local structure of the Zn- and Mn-codoped sample after annealing obtained by Fe-K XAFS is shown in Fig. 8(a). The first-nearest-neighbor bond is Fe–O and is distributed around $r \sim 1.5$ Å. The second-nearest-neighbor bond is Fe–Fe and is distributed around 3.5 Å. On the other hand, the second- and third-nearest-neighbor bonds of the Mn-doped sample, distributed around 2.2 and 3.1 Å, respectively, are Fe–Bi, as shown in Fig. 8(b). The peak corresponding to the Fe–Fe bond has lower amplitude for the Mn-doped annealed sample than for the Zn- and Mn-codoped samples after annealing. The fitting of the Bi-$L3$ XAFS spectrum was also analyzed in the same manner. The results for the Zn- and Mn-codoped and Mn-doped samples are shown in Figs. 8(c) and 8(d), respectively. In the Zn- and Mn-codoped sample, the second-nearest-neighbor bond is Bi–O and is distributed around 2.1 Å. In the Mn-doped sample, the peak corresponding to the Bi–O bond had a lower intensity and the Bi–Fe bond distribution around 2.8 Å became the second-nearest-neighbor peak.

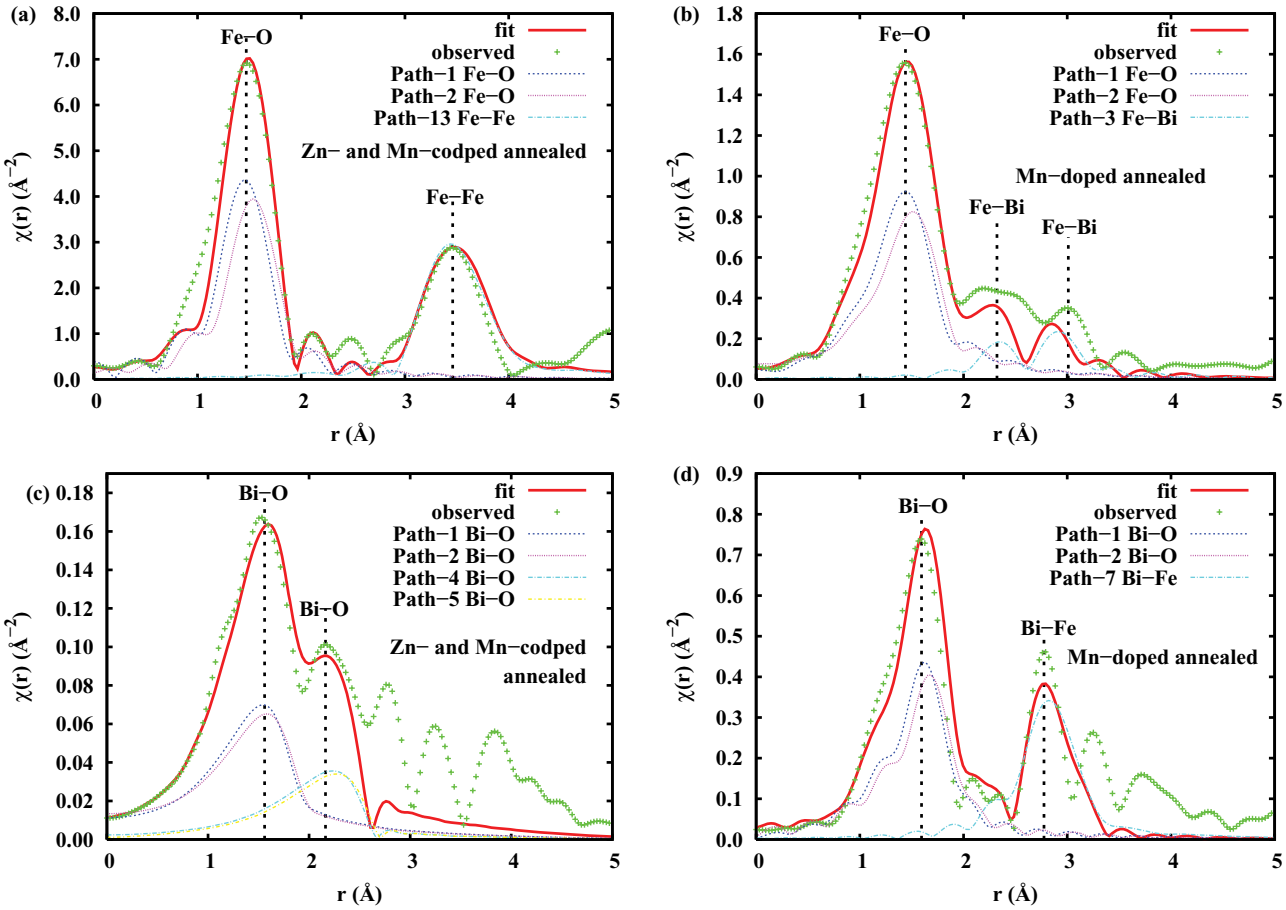

FIG. 8. (Color) Fourier transforms of (a) Zn- and Mn-codoped and (b) Mn-doped $BiFeO_3$ after annealing obtained by Fe-K XAFS. Fourier transforms of (c) Zn- and Mn-codoped and (d) Mn-doped $BiFeO_3$ after annealing obtained by Bi-$L3$ XAFS. The observed and fit data are shown by crosses and thick solid lines, respectively. The fit data are the sum of the paths shown by thin dashed lines.

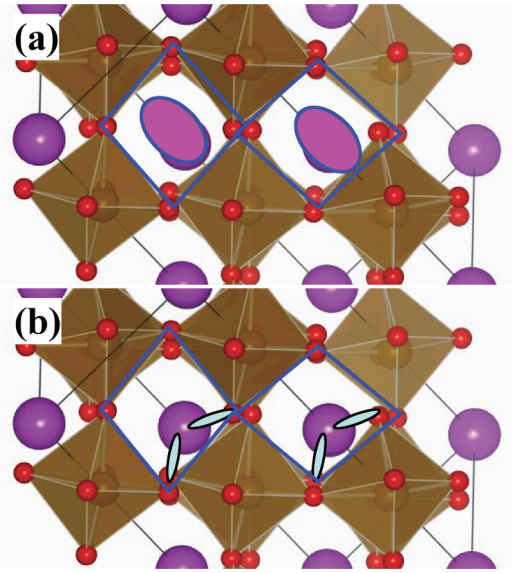

FIG. 9. (Color online) Schematic diagram of local structures of (a) Zn- and Mn-codoped $BiFeO_3$ and (b) Mn-doped $BiFeO_3$. In Zn- and Mn-codoped $BiFeO_3$, Bi ions are disordered from the rhombohedral lattice points. In Mn-doped $BiFeO_3$, Bi ions are stabilized owing to Bi–O hybridization.

In Zn- and Mn-codoped $BiFeO_3$, the perovskite units are stabilized because larger Zn^{2+} and Mn^{2+} ions are substituted for smaller Fe^{3+} ions. Since rhombohedral FeO_6 framework are disordered by the substitution of the larger Zn^{2+} and Mn^{2+} ions, Bi ions are located towards the free space in the BiO_{12} cages, as shown in Fig. 9(a). As a result, shorter and longer Bi–O bonds are observed as the first- and second-nearest-neighbor bond distributions, respectively, as shown in Fig. 8(c). In Mn-doped $BiFeO_3$, the perovskite units are still unstable because Mn^{3+} ions are substituted for Fe^{3+} ions of the same size. Then, Fe^{3+} ions change to Fe^{2+} owing to charge transfer from the Bi ions. Bi coordination increases as Bi–O hybridization changes. As a result, the shorter Bi–O correlation becomes strong, as shown in Fig. 9(b). On the other hand, the longer Bi–O bonds cannot be correlated in the rhombohedral FeO_6 framework in the Mn-doped $BiFeO_3$ sample, as shown in Fig. 8(d)

IV. DISCUSSION

We prepared the Zn- and Mn-codoped $BiFeO_3$ and Mn-doped $BiFeO_3$ crystals with the aim of enhancing ferroelectric properties. The low leakage current indicates the oxygen and Bi deficiencies are quite few. In such $BiFeO_3$ crystals, valence states of doping materials are important to control the ferroelectric properties. Essentially, pure $BiFeO_3$ has a well small P_s owing to its large E_c. We expected that doped ions would act as nuclei in domain switching. Actually, a large P_s was observed in the doped $BiFeO_3$ crystals, as shown in Fig. 2(a). The doped ions affected not only the ferroelectric properties but also the magnetic properties, as shown in Fig. 3(b). The magnetic properties show that the substitution effect of Zn- and Mn-codoped $BiFeO_3$ was larger than that of Mn-doped $BiFeO_3$. The substitution effect appeared as a decrease in the Néel temperature of Zn- and Mn-codoped $BiFeO_3$. Zn- and Mn-codoped $BiFeO_3$ also had a larger P_s than Mn-doped $BiFeO_3$. This is also evidence that the doped ions of Zn- and Mn-codoped $BiFeO_3$ have a substitution effect, as expected. We performed XAFS and XES measurements to clarify the electronic and local structures of the doped $BiFeO_3$ crystals.

The XAFS and XES measurements revealed that the difference between the Zn- and Mn-codoped and Mn-doped $BiFeO_3$ crystals was very small before annealing. We here discuss the change in the electronic and local structures of these samples due to annealing. We clarified that Mn was substituted as Mn^{2+} in Zn- and Mn-codoped annealed $BiFeO_3$ and that most of Mn was substituted as Mn^{3+} and part was substituted as Mn^{2+} in the other three samples, as shown in Fig. 4. When hole conductivity exists owing to oxygen vacancies, Mn^{2+} changes to Mn^{3+}. As a result, Mn^{2+} acts as a hole acceptor and the leakage current decreases. Before annealing, oxygen deficiency exists and causes hole conductivity, with the same manner as mentioned in Zn-doped $BiFeO_3$. Thus the doped Mn ion acts as a hole acceptor and exists as Mn^{3+} in both the Zn- and Mn-codoped and Mn-doped as-grown samples. When there are few oxygen vacancies, the Mn valence state is affected by another factor. Mn^{2+} can only exist when the leakage current is small. The number of oxygen vacancies was reduced by annealing, but the Mn valence of the annealed samples exhibits different behavior in the Zn- and Mn-codoped and Mn-doped samples. To explain this discrepancy, we introduce the concept of phonon-electron coupling similar to that in strongly electron correlated systems.

The $BiFeO_3$ perovskite unit is not stable owing to its small tolerance factor. Thus the *B*-site ion requires a large space to maintain the perovskite unit. Before annealing, a repulsion force owing to the oxygen vacancies should exist, which maintains the perovskite unit. After annealing, the repulsion force disappeared, but the perovskite unit was still maintained by the larger ionic radius of the substituted Zn^{2+} and Mn^{2+} in Zn- and Mn-codoped annealed $BiFeO_3$. Since the perovskite unit was stabilized in Zn- and Mn-codoped annealed $BiFeO_3$, the Fe–Fe correlation became strong, as shown in Fig. 8(a). When the *B*-site ions are substituted by larger ions, the rhombohedral distortion is relaxed and the free volume around the Bi ions increases. As a result, the Bi ions of Zn- and Mn-codoped $BiFeO_3$ are distributed toward the oxygen atoms involved in the longer Bi–O bonds, as shown in Fig. 9(a). The substitution effect was large owing to the heterovalent substitution of Mn^{2+}, which has a different ionic radii from Fe^{3+}. Moreover, the *A* site also has large randomness owing to the disordering feature of Bi ions. The large randomness facilitates domain switching. The large remanent polarization and the rapid increase in magnetization at low temperatures for Zn- and Mn-codoped $BiFeO_3$ are caused by these substitution effects.

In Mn-doped annealed $BiFeO_3$, most of the substituted Mn exists as Mn^{3+}. Since Fe^{3+} and Mn^{3+} are the same ionic size, a small tolerance still remained and the perovskite unit was still unstable. The perovskite unit was maintained by changing the Fe–O bond distance, as shown in Table II. In such an unstable perovskite, the Fe–Fe correlation became weaker than the Fe–Bi correlation, as shown in Fig. 8(b). The small tolerance around the Bi ion is relaxed by changing the Fe–O–Bi hybridization. Actually, the Bi-*L*3 XAFS

measurements revealed that the electronic structure of the Bi ion changed with the change in the Bi–O hybridization, as shown in Fig. 6. The Bi ions remained at the rhombohedral lattice points owing to Bi–O covalent bonding. The evidence of Fe–O–Bi hybridization was also observed in Fe pre-edge peak, as shown in Fig. 5(b). The behaviors of the *B*-site atoms are closely connected with the electronic structure of the *A*-site atom of Bi. Since the Bi 6*s* and O 2*p* hybridization should become strong, the electronic structure of Bi is easily affected by *B*-site atoms. The local structure around Bi atoms is also changed with changes in the electronic structure owing to the hybridization between Bi 6*s*, O 2*p*, and Fe, Mn 3*d* states. The XAFS measurements using the Bi-*L*3 edge also revealed that the electronic and local structures of the as-grown Zn- and Mn-codoped and Mn-doped $BiFeO_3$ crystals are very similar but they changed during the annealing process, because Mn plays different role before and after annealing.

Mn substitution has two different effects on $BiFeO_3$. When hole concentration is very high, the substituted Mn acts as a hole acceptor. When hole conductivity is sufficient low, the substituted Mn ensures structural stability. Before annealing, hole conductivity exists owing to the oxygen deficiency, and most Mn ions act as hole acceptors. After annealing, the hole conductivity is sufficiently reduced for Mn ions to mainly have the role of ensuring structural stability. However, this cannot explain the leakage properties only observed in the Mn valence state. The leakage properties depend on the Fe^{2+}/Fe^{3+} ratio in the annealed samples. In Zn- and Mn-codoped $BiFeO_3$, larger Zn^{2+} and Mn^{2+} ions are substituted for smaller Fe^{3+} ions. The perovskite unit becomes stable owing to the existence of the substituted larger ions. The Fe valence state is +3 in Zn- and Mn-codoped $BiFeO_3$, and the leakage current is generated by the heterovalent Zn^{2+} and Mn^{2+} ions. In Mn-doped annealed $BiFeO_3$, homovalent Mn^{3+} ions are substituted for Fe^{3+}. The perovskite unit remains unstable when Mn^{3+} ions are substituted for Fe^{3+} ions of the same size. The electronic structure of Bi is also affected when the *B*-site environment changes owing to the Bi 6*s*–O 2*p*–Fe 3*d* hybridization. The XES measurement revealed that the Fe^{2+} ion still exists in annealed Mn-doped $BiFeO_3$, as shown in Fig. 7(d). The Fe^{3+} ion changed to Fe^{2+} by charge transfer from the O 2*p* state. The evidence of charge transfer is the local structure of Bi and pre-edge peak of Fe. These evidences can be observed in the Mn-doped annealed sample. The origin of leak current in Mn-doped annealed sample is oxygen vacancy. Since the local structure around Bi changed owing to charge transfer, recombination of oxygen by the annealing should be interrupted. The oxygen ion hybridizes both Bi and Fe. As a result, the Fe^{3+} ion changed to Fe^{2+} by charge transfer from the Bi ion. The Bi ion delivers one electron by changing its electronic and local structures. Thus the conductivity of Mn-doped $BiFeO_3$ is caused by the charge transfer similarly to in the $BiNiO_3$ system.[39] This oxide is not a simple Ni 3*d* → O 2*p* system but a Bi 6*s*–Ni 3*d*–O 2*p* electronic system. $BiNiO_3$ undergoes a metal-insulator (MI) transition upon applying a high pressure of 4 GPa. The pressure-induced MI transition is caused by the melting of Bi-charge disproportionation and simultaneous Ni → Bi charge transfer: $Bi^{3+}_{0.5}Bi^{5+}_{0.5}Ni^{2+}O_3 \rightarrow Bi^{3+}Ni^{3+}O_3$.[40] In $BiNiO_3$, the local environment of Bi is changed by the application of pressure, whereas in $BiFeO_3$, the local environment of Bi is changed by substitution. The difference between the leakage properties of the Zn- and Mn-codoped and Mn-doped $BiFeO_3$ crystals can be explained by a kind of MI transition owing to Fe → Bi charge transfer.

V. CONCLUSIONS

We have presented the electronic and local structures of Zn- and Mn-codoped and Mn-doped $BiFeO_3$ crystals obtained using XAFS and XES data. The XAFS analysis of *B*-site ions of the perovskite unit indicates that the substituted Mn ions have two roles: one is as a hole acceptor and the other is to ensure the stability of the perovskite structure. When many oxygen vacancies exist, the substituted Mn act as a hole acceptor, then Mn exists in the +3 oxidation state. On the other hand, the substituted Mn stabilizes the structure when there are few oxygen vacancies. In Zn- and Mn-codoped $BiFeO_3$, the perovskite unit is stabilized by substituting the larger Zn^{2+} and Mn^{2+} ions for the smaller Fe^{3+} ion. However, this cannot explain the leakage properties, which only depend on the valence state of the substituted Mn. The electronic structure of the host Fe is also affected by the substitution. XES revealed that Fe^{2+} still existed in annealed Mn-doped $BiFeO_3$ despite the small number of oxygen vacancies. Although Mn is doped in the *B*-site, the *A*-site atom of Bi is also affected by the substitution. We proposed the charge transfer of Bi → Fe owing to the Bi 6*s*–O 2*p*–Fe 3*d* hybridization.

ACKNOWLEDGMENTS

Y. Itoh of Kyoto University, A. Nisawa of RIKEN, and S. Fukushima of National Institute for Material Science (NIMS) are acknowledged for their help in the data collection by XES and data reduction. The authors thank A. Belik of NIMS for providing high-quality $BiMnO_3$ reference samples and also thank to Y. Takeda and K. Yoshii of JAEA for fruitful discussion on magnetic measurements. This work was supported by a Grant-in-Aid (No. 22604006) from the Ministry of Education, Culture, Sports, Science and Technology. The XAFS measurements were performed at the facilities of BL14B1 (Proposal Nos. 2010A3608 and 2010B3608) in SPring-8.

*yoneda@spring8.or.jp

[1] A. Singh, A. Senyshyn, H. Fuess, T. Chatterji, and D. Pandey, Phys. Rev. B **83**, 054406 (2011).

[2] D. C. Arnold, K. S. Knight, G. Catalan, S. A. T. Redfern, J. F. Scott, P. Lightfoot, and F. D. Morrison, Adv. Funct. Mater. **20**, 1 (2010).

[3] Y. P. Wang, L. Zhou, M. F. Zhang, X. Y. Chen, J. M. Liu, and Z. G. Liu, Appl. Phys. Lett. **84**, 1731 (2004).

[4] V. R. Palker and R. Pinto, Pramana-J. Phys. **58**, 1003 (2002).

[5] Y. Noguchi, Y. Kitanaka, and M. Miyayama, Butsuri **65**, 769 (2010). (in Japanese)

[6]M. Li and J. L. MacManus-Driscoll, Appl. Phys. Lett. **87**, 252510 (2005).
[7]R. C. Miller and G. Weinreich, Phys. Rev. **117**, 1460 (1960).
[8]D. Viehland and Y. H. Chen, J. Appl. Phys. **88**, 6696 (2000).
[9]Y. Chishima, Y. Noguchi, Y. Kitanaka, and M. Miyayama, IEEE Trans. Ultrason. Ferroelectr. Freq. Control **57**, 2233 (2010).
[10]W. Hai, H. Haitao, and W. Biao, Sci. Adv. Mater. **2**, 184 (2010).
[11]S. M. Selbach, T. Tybell, M.-A. Einarsrud, and T. Grande, Chem. Mater. **21**, 5176 (2009).
[12]S. M. Selbach, T. Tybell, M.-A. Einarsrud, and T. Grande, Phys. Rev. B **79**, 214113 (2009).
[13]D. Kothari, V. R. Reddy, A. Gupta, D. M. Phase, N. Lakshmi, S. K. Deshpande, and A. M. Awasthi, J. Phys.: Condens. Matter **19**, 136202 (2007).
[14]T. Higuchi, T. Hattori, W. Sakamoto, N. Itoh, T. Shimura, T. Yogo, P. Yao, Y.-S. Liu, P.-A. Glans, C. Chang, Z. Wu, and J. Guo, Jpn. J. Appl. Phys. **47**, 7570 (2008).
[15]M. Kumar and K. L. Yadav, Appl. Phys. Lett. **91**, 242901 (2007).
[16]G. Anjum, R. Kumar, S. Mollah, P. Thakur, S. Guntam, and K. H. Chae, J. Phys. D **44**, 075403 (2011).
[17]T. Kawae, Y. Terauchi, H. Tsuda, M. Kumeda, and A. Morimoto, Appl. Phys. Lett. **94**, 112904 (2009).
[18]T. Higuchi, W. Sakamoto, N. Itoh, T. Shimura, T. Hattori, and T. Yogo, Appl. Phys. Express **1**, 011502 (2008).
[19]Y. Yoneda and W. Sakamoto, J. Phys.: Condens. Matter **23**, 015902 (2011).
[20]J. Wu, J. Wang, D. Xiao, and J. Zhu, Appl. Surf. Sci. **257**, 7226 (2011).
[21]Y. Yoneda, N. Matsumoto, Y. Furukawa, and T. Ishikawa, J. Synchrotron Radiat. **8**, 18 (2001).
[22]M. Newville, J. Synchrotron Radiat. **8**, 322 (2001).
[23]B. Raval and M. Newville, J. Synchrotron Radiat. **12**, 547 (2005).
[24]T. Tochio, Y. Ito, and K. Omote, Phys. Rev. A **65**, 042502 (2002).
[25]K. Momma and F. Izumi, J. Appl. Crystallogr. **44**, 1272 (2011).
[26]W. L. Warren, J. Robertson, D. B. Diomis, B. A. Tuttle, and D. M. Smyth, Ferroelectrics **153**, 303 (1994).
[27]A. A. Belik and E. Takayama-Muromachi, Inorg. Chem. **46**, 5585 (2007).
[28]A. A. Belik, T. Yokosawa, K. Kimoto, Y. Matsui, and E. Takayama-Muromachi, Chem. Mater. **19**, 1679 (2007).
[29]A. A. Belik and E. Takayama-Muromachi, J. Phys.: Condens. Matter **20**, 025211 (2008).
[30]R. D. Shannon, Acta Crystallogr. Sect. A **32**, 751 (1976).
[31]T. Higuchi, Y.-S. Liu, P. Yao, P.-A. Glans, J. Guo, C. Chang, Z. Wu, W. Sakamoto, N. Itoh, T. Shimura, T. Yogo, and T. Hattori, Phys. Rev. B **78**, 085106 (2008).
[32]R. Sæterli, S. M. Selbach, P. Ravindran, T. Grande, and R. Holmestad, Phys. Rev. B **82**, 064102 (2010).
[33]J. Rodríguez-Carvajal, M. Hennion, F. Moussa, A. H. Moudden, L. Pinsard, and A. Revcolevschi, Phys. Rev. B **57**, R3189 (1998).
[34]M. Whangbo, H. Koo, A. Villesuzanne, and M. Pouchard, Inorg. Chem. **41**, 1920 (2002).
[35]R. V. Pisarev, A. S. Moskvin, A. M. Kalashnikova, and T. Rasing, Phys. Rev. B **79**, 235128 (2009).
[36]B. Ramachandran, A. Dixit, R. Naik, G. Lawes, and M. S. Ramachandra Rao, Phys. Rev. B **82**, 012102 (2010).
[37]J.-H. Lee, H. J. Choi, D. Lee, M. G. Kim, C. W. Bark, S. Ryu, M.-A. Oak, and H. M. Jang, Phys. Rev. B **82**, 045113 (2010).
[38]Y. Noguchi, T. Matsumoto, and M. Miyayama, Jpn. J. Appl. Phys. **44**, L570 (2005).
[39]M. Mizumaki, N. Ishimatsu, N. Kawamura, M. Azuma, Y. Shimakawa, M. Takano, and T. Uozumi, Phys. Rev. B **80**, 233104 (2009).
[40]M. Azuma, A. Fujimori, and Y. Tokura, Rev. Mod. Phys. **70**, 1039 (1998).